



## Article

# Enhanced Structural and Electrochemical Performance of LiNi<sub>0.5</sub>Mn<sub>1.5</sub>O<sub>4</sub> Cathode Material by PO<sub>4</sub><sup>3-</sup>/Fe<sup>3+</sup> Co-Doping

Yong Wang <sup>1</sup>, Shaoxiong Fu <sup>2</sup>, Xianzhen Du <sup>1</sup>, Dong Wei <sup>1</sup>, Jingpeng Zhang <sup>1,\*</sup>, Li Wang <sup>1,2,\*</sup> and Guangchuan Liang <sup>1,2</sup>

<sup>1</sup> Shandong Goldencell Electronics Technology Co., Ltd., Zaozhuang 277100, China; tec@goldencell.biz (Y.W.)

<sup>2</sup> School of Materials Science and Engineering, Hebei University of Technology, Tianjin 300401, China; 13931100462@163.com

\* Correspondence: tec03@goldencell.biz (J.Z.); wangli\_hebut@163.com (L.W.)

**Abstract:** Series of PO<sub>4</sub><sup>3-</sup>/Fe<sup>3+</sup> co-doped samples of LiNi<sub>0.5</sub>Mn<sub>1.5-5/3x</sub>Fe<sub>x</sub>P<sub>2/3x</sub>O<sub>4</sub> ( $x = 0.01, 0.02, 0.03, 0.04, 0.05$ ) have been synthesized by the coprecipitation-hydrothermal method, along with high-temperature calcination using FeSO<sub>4</sub> and NaH<sub>2</sub>PO<sub>4</sub> as Fe<sup>3+</sup> and PO<sub>4</sub><sup>3-</sup> sources, respectively. The effects of the PO<sub>4</sub><sup>3-</sup>/Fe<sup>3+</sup> co-doping amount on the crystal structure, particle morphology and electrochemical performance of LiNi<sub>0.5</sub>Mn<sub>1.5</sub>O<sub>4</sub> are intensively studied. The results show that the PO<sub>4</sub><sup>3-</sup>/Fe<sup>3+</sup> co-doping amount exerts a significant influence on the crystal structure and particle morphology, including increased crystallinity, lowered Mn<sup>3+</sup> content, smaller primary particle size with decreased agglomeration and the exposure of high-energy (110) and (311) crystal surfaces in primary particles. The synergy of the above factors contributes to the obviously ameliorated electrochemical performance of the co-doped samples. The LiNi<sub>0.5</sub>Mn<sub>1.45</sub>Fe<sub>0.03</sub>P<sub>0.02</sub>O<sub>4</sub> sample exhibits the best cycling stability, and the LiNi<sub>0.5</sub>Mn<sub>1.4333</sub>Fe<sub>0.04</sub>P<sub>0.0267</sub>O<sub>4</sub> sample displays the best rate performance. The electrochemical properties of LiNi<sub>0.5</sub>Mn<sub>1.5-5/3x</sub>Fe<sub>x</sub>P<sub>2/3x</sub>O<sub>4</sub> can be regulated by adjusting the PO<sub>4</sub><sup>3-</sup>/Fe<sup>3+</sup> co-doping amount.



**Citation:** Wang, Y.; Fu, S.; Du, X.; Wei, D.; Zhang, J.; Wang, L.; Liang, G. Enhanced Structural and Electrochemical Performance of LiNi<sub>0.5</sub>Mn<sub>1.5</sub>O<sub>4</sub> Cathode Material by PO<sub>4</sub><sup>3-</sup>/Fe<sup>3+</sup> Co-Doping. *Batteries* **2024**, *10*, 341. <https://doi.org/10.3390/batteries10100341>

Academic Editor: Yong-Joon Park

Received: 8 August 2024

Revised: 17 September 2024

Accepted: 24 September 2024

Published: 26 September 2024



**Copyright:** © 2024 by the authors. Licensee MDPI, Basel, Switzerland. This article is an open access article distributed under the terms and conditions of the Creative Commons Attribution (CC BY) license (<https://creativecommons.org/licenses/by/4.0/>).

## 1. Introduction

At present, lithium-ion batteries (LIBs) are widely adopted in portable electronic products, electric vehicles and energy storage equipment due to the advantages of high energy density, a long cycle life and high safety [1]. The capacity, energy density and cycling performance of LIBs mainly depend on the cathode material [2]. The current mainstream commercial cathode materials include LiCoO<sub>2</sub>, LiMn<sub>2</sub>O<sub>4</sub>, LiFePO<sub>4</sub> and LiNi<sub>x</sub>Co<sub>y</sub>Mn<sub>z</sub>O<sub>2</sub> ( $x + y + z = 1$ ) ternary material. The low energy density of LiMn<sub>2</sub>O<sub>4</sub>, the complex preparation technology of LiFePO<sub>4</sub> and the high cost of Co for LiCoO<sub>2</sub> and ternary material limit their further application in electric vehicles and energy storage equipment. Therefore, there is an urgent need to develop a cathode material with a higher energy density, higher safety and lower cost. As is well known, the energy density of LIBs is directly affected by that of the cathode material, which is the product of its specific discharge capacity and operation voltage. Therefore, finding a cathode material with a higher specific capacity or operation voltage can effectively improve the energy density of LIBs.

Spinel LiNi<sub>0.5</sub>Mn<sub>1.5</sub>O<sub>4</sub> (LNMO) has been regarded as a promising next-generation cathode material due to its high operation voltage of 4.7 V (vs. Li/Li<sup>+</sup>), high energy density of 650 Wh kg<sup>-1</sup>, fast Li<sup>+</sup> insertion/extraction kinetics and abundant raw materials [3,4]. However, LNMO usually exhibits rapid capacity fading, mainly originating from irreversible structure change, transition metal ion dissolution and side reactions with liquid electrolytes [3]. Many endeavors have been undertaken to alleviate the above problems,

such as surface coating and element doping. A surface coating using oxide [5], fluoride [6], phosphate [7] and other compounds ( $\text{LaFeO}_3$  [8],  $\text{Li}_{0.35}\text{La}_{0.55}\text{TiO}_3$  [9], etc.) has been applied to reduce side reactions with an electrolyte. Element doping is believed to be a cost-effective method to improve the structural stability and rate capability of a cathode material. In previous works, cations ( $\text{Na}^+$  [10],  $\text{Mg}^{2+}$  [11],  $\text{Cr}^{3+}$  [12],  $\text{Ru}^{4+}$  [13], etc.) and anions ( $\text{F}^-$  [14],  $\text{S}^{2-}$  [15],  $\text{Cl}^-$  [16], etc.) have been used to dope into the LNMO lattice to improve the electrochemical performance. Presently, much attention has been paid to cation or anion single-doping, which can only improve the specific aspect of electrochemical performance. Therefore, in consideration of the integrated advantages of cation and anion doping, the cation and anion co-doping strategy has been proposed to regulate the spinel structure of LNMO material.

On the other hand, because the polyanion bonds are stronger than TM-O (TM = Ni, Mn) bonds, polyanion doping ( $\text{PO}_4^{3-}$ ,  $\text{BO}_4^{5-}$ ,  $\text{SiO}_4^{4-}$ , etc.) has been used to enhance the electrochemical performance of Ni-rich and Li-rich cathode materials [17–19]. However, until now, there are few reports on polyanion doping modification on  $\text{LiNi}_{0.5}\text{Mn}_{1.5}\text{O}_4$  material. In our previous work [20], it was found that a  $\text{PO}_4^{3-}/\text{Fe}^{3+}$  co-doped sample exhibited better electrochemical performance than un-doped and single-doped samples. Herein, a series of  $\text{PO}_4^{3-}/\text{Fe}^{3+}$  co-doped samples of  $\text{LiNi}_{0.5}\text{Mn}_{1.5-5/3x}\text{Fe}_x\text{P}_{2/3x}\text{O}_4$  ( $x = 0.01, 0.02, 0.03, 0.04, 0.05$ ) were synthesized via the coprecipitation–hydrothermal method together with two-step calcinations using  $\text{FeSO}_4$  as an  $\text{Fe}^{3+}$  source and  $\text{NaH}_2\text{PO}_4$  as a  $\text{PO}_4^{3-}$  source. The influence of the  $\text{PO}_4^{3-}/\text{Fe}^{3+}$  co-doping amount on the structure, particle morphology and electrochemical properties of  $\text{LiNi}_{0.5}\text{Mn}_{1.5}\text{O}_4$  are intensively studied.

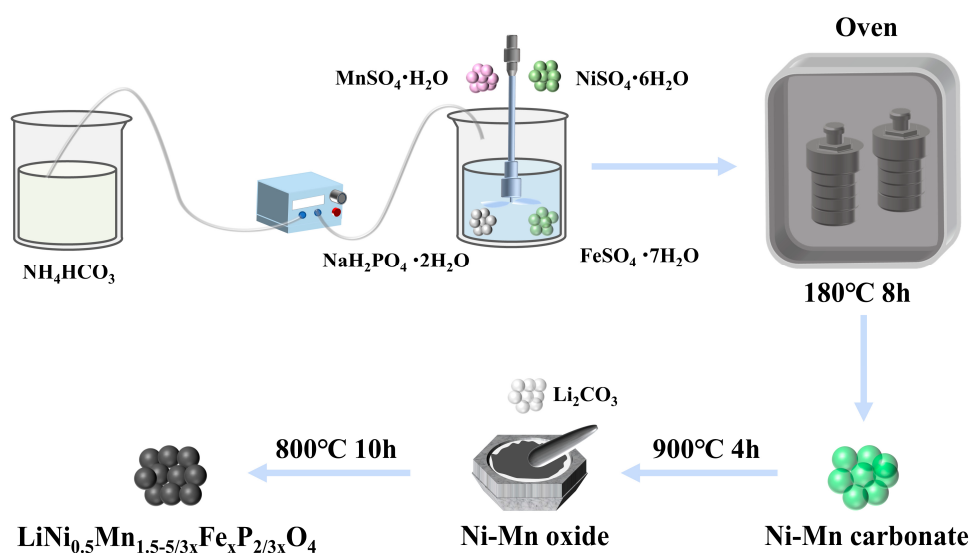
## 2. Materials and Methods

### 2.1. Material Synthesis

The preparation process of a  $\text{PO}_4^{3-}/\text{Fe}^{3+}$  co-doped sample is illustrated in Scheme 1. Firstly, a coprecipitation–hydrothermal method was adopted to prepare a  $\text{PO}_4^{3-}/\text{Fe}^{3+}$  co-doped carbonate precursor by using  $\text{FeSO}_4$  and  $\text{NaH}_2\text{PO}_4$  as  $\text{Fe}^{3+}$  and  $\text{PO}_4^{3-}$  sources, respectively. To be specific, according to the formula  $\text{LiNi}_{0.5}\text{Mn}_{1.5-5/3x}\text{Fe}_x\text{P}_{2/3x}\text{O}_4$  ( $x = 0.01, 0.02, 0.03, 0.04, 0.05$ ), 0.6 mmol  $\text{FeSO}_4 \cdot 7\text{H}_2\text{O}$  (99.0%, ShengAo, Tianjin, China) and 0.4 mmol  $\text{NaH}_2\text{PO}_4 \cdot 2\text{H}_2\text{O}$  (99.0%, BoDi, Tianjin, China) were added to a mixture of deionized water (160 mL) and ethylene glycol (80 mL). After 30 min of stirring,  $\text{NiSO}_4 \cdot 6\text{H}_2\text{O}$  (15 mmol, 99%, DaMao) and  $\text{MnSO}_4 \cdot \text{H}_2\text{O}$  (45 mmol, 99%, GuangFu, Tianjin, China) were added and stirred for 30 min to obtain a metal salt solution.  $\text{NH}_4\text{HCO}_3$  (300 mmol, 99%, FuChen, Tianjin, China) was totally dissolved in deionized water (160 mL), and the obtained solution was added to the above metal salt solution via a peristaltic pump. After stirring for 30 min, the resulting suspension was placed into a Teflon-lined stainless-steel autoclave and maintained at 180 °C for 8 h in a blast oven. After cooling, repeated filtering and washing, the resultant  $\text{PO}_4^{3-}/\text{Fe}^{3+}$  co-doped carbonate powder was pre-sintered in a muffle furnace at 900 °C for 4 h to obtain a black oxide powder, which was uniformly blended with 5 wt.% excess  $\text{Li}_2\text{CO}_3$  and sintered at 800 °C for 10 h. After sieving through a 325-mesh sieve the final  $\text{LiNi}_{0.5}\text{Mn}_{1.5-5/3x}\text{Fe}_x\text{P}_{2/3x}\text{O}_4$  ( $x = 0.01, 0.02, 0.03, 0.04, 0.05$ ) products were achieved and named as LNMO-FeP0.01, LNMO-FeP0.02, LNMO-FeP0.03, LNMO-FeP0.04, LNMO-FeP0.05, respectively. For comparison, the un-doped LNMO sample was synthesized based on the above process but with the absence of  $\text{FeSO}_4 \cdot 7\text{H}_2\text{O}$  and  $\text{NaH}_2\text{PO}_4 \cdot 2\text{H}_2\text{O}$ .

### 2.2. Material Characterization

The crystal structure was analyzed using an X-ray diffractometer (XRD, Smartlab 9KW, Rigaku, Japan) using  $\text{CuK}\alpha$  radiation in the range of  $2\theta = 10\text{--}80^\circ$  and Fourier transform infrared spectroscopy (FT-IR, V80, Bruker, Germany) in the range of  $700\text{--}400\text{ cm}^{-1}$ . Scanning electron microscopy (SEM, JSM-7610F, Japan) was used to observe the particle morphology.



**Scheme 1.** Illustration of preparation process for  $\text{PO}_4^{3-}/\text{Fe}^{3+}$  co-doped sample.

### 2.3. Electrochemical Tests

CR2032 coin-type cells were assembled in an Ar-filled glove box, which consists of a cathode sheet, lithium metal anode, Celgard 2400 microporous membrane and commercial electrolyte purchased from Tinci Company. The cathode sheet was prepared as follows: LNMO powder, polyvinylidene fluoride (PVDF) and Super P (weight ratio 8:1:1) were mixed uniformly in N-methyl-2-pyrrolidone (NMP) to obtain a slurry, which was casted on aluminum foil using a doctor blade. After vacuum desiccation, the resultant Al foil was cut into 12 mm diameter round sheets. The constant-current charge/discharge tests were measured between 3.5 and 4.95 V at 25 °C on a Land battery test system (CT2001A, Wuhan, China). Cyclic voltammetry (CV) and electrochemical impedance spectroscopy (EIS) tests were conducted on the electrochemical workstation (CHI660E, Chenhua, Shanghai, China) using a two-electrode system. An EIS test was conducted in the frequency range of 100 kHz–100 mHz with a 5 mV amplitude.

## 3. Results and Discussion

Figure 1a shows the XRD patterns of the pristine LNMO and co-doped  $\text{LiNi}_{0.5}\text{Mn}_{1.5-5/3x}\text{Fe}_x\text{P}_{2/3x}\text{O}_4$  samples. For all samples, the diffraction peaks can be ascribed to an  $Fd\bar{3}m$  cubic spinel  $\text{LiNi}_{0.5}\text{Mn}_{1.5}\text{O}_4$  (PDF #80-2162), and the sharp and narrow diffraction peaks suggest a well-crystallized spinel structure for all samples. The absence of impurity diffraction peaks also suggests that the  $\text{Fe}^{3+}$  and  $\text{PO}_4^{3-}$  ions have been successfully doped into the spinel lattice without changing the crystal structure of the LNMO material. The high phase purity contributes to less side reactions and the ameliorated electrochemical performance of the LNMO material. In contrast, the peak intensities of the co-doped samples are obviously increased in comparison with the un-doped sample, implying enhanced crystallinity after  $\text{PO}_4^{3-}/\text{Fe}^{3+}$  co-doping, which also benefits the electrochemical performance of the co-doped samples.

Jade 6.5 software was adopted to refine the XRD patterns, and the refined lattice constants  $a$  for the LNMO, LNMO-FeP0.01, LNMO-FeP0.02, LNMO-FeP0.03, LNMO-FeP0.04 and LNMO-FeP0.05 samples are 8.1804 Å, 8.1738 Å, 8.1640 Å, 8.1625 Å, 8.1597 Å and 8.1574 Å, respectively. It is evident that the lattice constants show a gradually decreasing trend with the  $\text{PO}_4^{3-}/\text{Fe}^{3+}$  co-doping amount increasing. This is primarily attributed to the P-O (410 kJ mol<sup>-1</sup>, 298 K) and Fe-O (409 kJ mol<sup>-1</sup>, 298 K) bonds being stronger than the Ni-O (392 kJ mol<sup>-1</sup>, 298 K) and Mn-O (402 kJ mol<sup>-1</sup>, 298 K) bonds, which can reduce oxygen evaporation during the calcination process, thus generating less  $\text{Mn}^{3+}$  ions to keep the charge neutrality. In consideration of the smaller ionic radius of  $\text{Mn}^{4+}$  (0.530 Å) compared

with  $Mn^{3+}$  (0.645 Å), the increasing co-doping amount leads to the gradually decreased  $Mn^{3+}$  content, thereby inducing the gradually decreasing lattice constants. Figure 1b shows the magnified pattern of the (111) peak, where we observe that the (111) peak gradually shifts to higher angles along with the increase in the co-doping amount, in good correspondence with the gradually decreasing lattice constants. The shift of the (111) peak after  $PO_4^{3-}/Fe^{3+}$  co-doping also suggests their successful incorporation into the spinel lattice.

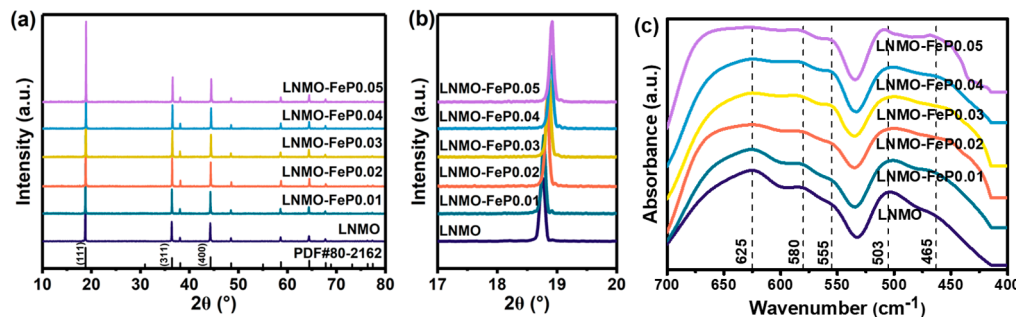


**Figure 1.** XRD patterns (a) and magnified pattern of (111) peak (b) and FT-IR spectra (c) of all samples.

As mentioned previously, for  $LiNi_{0.5}Mn_{1.5}O_4$  materials, the higher the  $I_{311}/I_{400}$  peak intensity ratio is, the better the structural stability is [21]. According to Figure 1a, the calculated  $I_{311}/I_{400}$  intensity ratios for the LNMO, LNMO-Fe0.01, LNMO-FeP0.02, LNMO-FeP0.03, LNMO-FeP0.04 and LNMO-FeP0.05 samples are 1.071, 1.104, 1.170, 1.181, 1.142 and 1.084, respectively. That is, the enhanced  $I_{311}/I_{400}$  ratios of the co-doped samples imply improved structural stability and cycling stability after  $PO_4^{3-}/Fe^{3+}$  co-doping, mainly due to the higher bonding strength of the Fe-O and P-O bonds. Among the co-doped samples, the LNMO-FeP0.03 sample has the highest  $I_{311}/I_{400}$  ratio, suggesting that it has the best cycling capability. However, further increasing the co-doping amount to  $x = 0.05$  leads to a decrease in the  $I_{311}/I_{400}$  ratio, maybe due to the lattice distortion resulting from the excessive doping of  $PO_4^{3-}/Fe^{3+}$  ions.

In addition, the relative peak intensity in the XRD pattern can reflect the relative exposure of crystal planes [22]. In order to analyze the changes in the exposed crystal planes of samples, the relevant diffraction peaks were normalized to the (111) peak to explore the effect of  $PO_4^{3-}/Fe^{3+}$  co-doping on the selective growth of the (440) and (311) planes, and the obtained  $I_{440}/I_{111}$  and  $I_{311}/I_{111}$  intensity ratios are listed in Table 1. It is found that appropriate  $PO_4^{3-}/Fe^{3+}$  co-doping ( $x \leq 0.04$ ) can enhance the  $I_{440}/I_{111}$  and  $I_{311}/I_{111}$  intensity ratios, whereas overmuch co-doping ( $x = 0.05$ ) decreases the ratios again. That is, appropriate  $PO_4^{3-}/Fe^{3+}$  co-doping can increase the proportion of exposed (110) and (311) crystal planes. The changes in exposed crystal planes after  $PO_4^{3-}/Fe^{3+}$  co-doping can also be observed from Figure 2.

**Table 1.**  $I_{440}/I_{111}$  and  $I_{311}/I_{111}$  intensity ratios for un-doped and co-doped samples.

Sample	$I_{440}/I_{111}$	$I_{311}/I_{111}$
LNMO	0.0857	0.312
LNMO-FeP0.01	0.0862	0.313
LNMO-FeP0.02	0.0871	0.314
LNMO-FeP0.03	0.0895	0.321
LNMO-FeP0.04	0.0967	0.328
LNMO-FeP0.05	0.0870	0.309

$LiNi_{0.5}Mn_{1.5}O_4$  material generally displays two different crystal structures, including a disordered  $Fd3m$  structure and an ordered  $P4_{3}32$  structure [23], which can be distinguished by means of FT-IR, and the corresponding spectra are shown in Figure 1c. Generally, the ordered structure usually has eight absorption peaks, while the disordered one only has

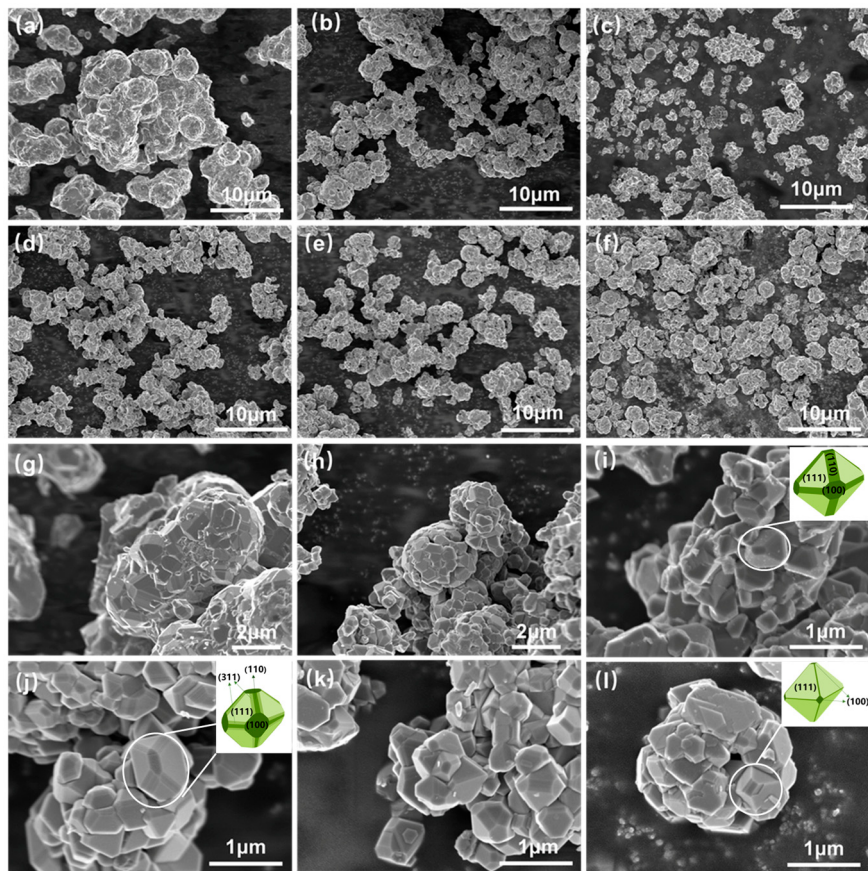
five broadened absorption peaks [24]. From Figure 1c, all samples exhibit five broadened absorption peaks at 625, 580, 555, 503 and  $465\text{ cm}^{-1}$ , manifesting the dominant disordered *Fd3m* structure. As is widely accepted, the disordered structure usually exhibits higher electronic conductivity than the ordered one because of the presence of  $\text{Mn}^{3+}$  [25]. In addition, from Figure 1c, the  $625\text{ cm}^{-1}$  absorption peak is stronger than the  $580\text{ cm}^{-1}$  absorption peak, also suggesting a dominant disordered *Fd3m* structure [21]. At the same time, the Ni/Mn disordering degree can be evaluated by the ratio of the  $625\text{ cm}^{-1}$  peak to the  $580\text{ cm}^{-1}$  peak ( $I_{625}/I_{580}$ ), and a higher  $I_{625}/I_{580}$  ratio usually means a higher degree of Ni/Mn disordering [26]. According to Figure 1c, the  $I_{625}/I_{580}$  intensity ratios of the LNMO, LNMO-Fe0.01, LNMO-FeP0.02, LNMO-FeP0.03, LNMO-FeP0.04 and LNMO-FeP0.05 samples are 1.193, 1.143, 1.054, 1.021, 1.020 and 1.018, respectively. In other words, the degree of Ni/Mn disordering ( $\text{Mn}^{3+}$  content) gradually decreases with the co-doping amount. In our previous work [20], the XPS analysis results of un-doped LNMO and co-doped LNMO-FeP0.02 samples also verify the decreased  $\text{Mn}^{3+}$  content in the LNMO-FeP0.02 sample. In addition, the XPS results imply that  $\text{Fe}^{3+}$  and  $\text{PO}_4^{3-}$  ions have been successfully doped into the LNMO-FeP0.02 lattice.

Figure 2 shows SEM images of the un-doped and co-doped samples. From Figure 2a,g, we observe that un-doped LNMO displays a secondary microspherical structure constituted by truncated octahedral primary particles with poor crystallinity and severe agglomeration, which may affect the  $\text{Li}^+$  ion insertion/extraction process, which is detrimental to the electrochemical properties of the LNMO material.

From Figure 2b,h, LNMO-FeP0.01 shows a similar particle morphology to un-doped LNMO but with improved crystallinity and reduced agglomeration. At a co-doping amount of  $x = 0.02$  (Figure 2c,i), the particle morphology and size of the LNMO-FeP0.02 sample change greatly, and most microsphere particles are replaced by dispersed small particles with greatly decreased primary particle sizes. Besides the (111) and (100) planes, a (110) plane also appears. The emergence of small dispersed particles with high-energy (110) crystal planes is mainly attributed to the enhanced crystal stability caused by the stronger Fe-O and P-O bonds, which allows the particles to exist as small dispersed particles with additional (110) planes.

When  $x = 0.03$  and 0.04, the primary particle size becomes smaller, as shown in Figure 2j,k. However, differently from LNMO-FeP0.02, the primary particles of LNMO-FeP0.03 and LNMO-FeP0.04 agglomerate together to reduce the total surface energy. And as seen from Figure 2j,k, the primary particles even exhibit a (311) plane besides the (111), (100) and (110) planes, which is induced by the synergistic effect of  $\text{PO}_4^{3-}/\text{Fe}^{3+}$  co-doping. When  $x$  further increases to 0.05, as shown in Figure 2f,l, primary LNMO-FeP0.05 particles agglomerate into the secondary microsphere structure, and the (311) and (110) planes decrease or even disappear. This may be due to the fact that excessive  $\text{PO}_4^{3-}/\text{Fe}^{3+}$  doping may cause lattice distortion, which in turn destroys the stability of the crystal structure.

Figure 3a shows the first-cycle charge/discharge curves of the un-doped and co-doped samples at a 0.2 C rate. The first specific discharge capacities at the 0.2 C rate are 120.0, 131.4, 134.5, 134.6, 145.2 and  $130.6\text{ mAh g}^{-1}$ , respectively, for LNMO, LNMO-Fe0.01, LNMO-FeP0.02, LNMO-FeP0.03, LNMO-FeP0.04 and LNMO-FeP0.05. That is, the first specific discharge capacities are increased after co-doping because of the improved crystallinity, decreased primary particle size and agglomeration, as well as the appearance of high-energy crystal planes. The emergence of high-energy (110) and (311) crystal planes contribute to LNMO-FeP0.04 having the highest first discharge capacity.



**Figure 2.** SEM images of all samples: (a,g) LNMO, (b,h) LNMO-FeP0.01, (c,i) LNMO-FeP0.02, (d,j) LNMO-FeP0.03, (e,k) LNMO-FeP0.04, (f,l) LNMO-FeP0.05.

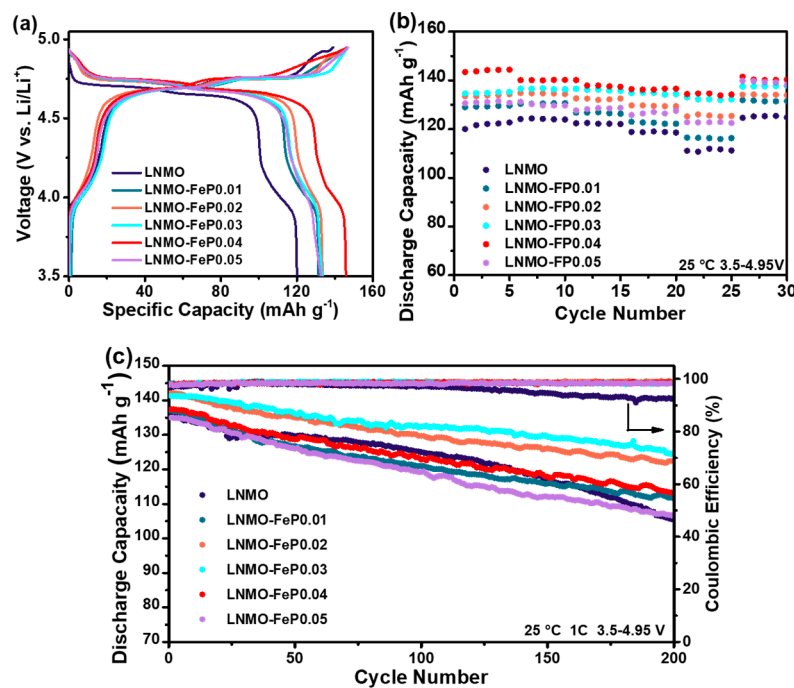


**Figure 3.** First-cycle charge/discharge curves at 0.2 C rate (a), rate capability curves (b) and cycling and coulombic efficiency curves (c) for all samples.

In addition, the ~4.7 V and ~4.0 V plateaus in the charge/discharge curves of all samples can be separately ascribed to  $\text{Ni}^{2+}/\text{Ni}^{4+}$  and  $\text{Mn}^{3+}/\text{Mn}^{4+}$  redox couples. The presence of a ~4.0 V plateau also confirms the dominant disordered structure, consistent with the above FT-IR results. In addition, the relative  $\text{Mn}^{3+}$  contents can be evaluated by the discharge capacity between 3.8 and 4.25 V divided by the total discharge capacity according to the first-cycle discharge curves [27], which are 14.83%, 11.47%, 9.37%, 9.21%, 8.92% and 8.03%, respectively, for LNMO, LNMO-Fe0.01, LNMO-FeP0.02, LNMO-FeP0.03, LNMO-FeP0.04 and LNMO-FeP0.05. That is, the  $\text{Mn}^{3+}$  content gradually decreases with the co-doping amount, due to the fact that the stronger Fe-O and P-O bonds reduce oxygen loss during calcination and then result in the formation of fewer  $\text{Mn}^{3+}$  ions.

Figure 3b shows the rate capability curves of the un-doped and co-doped samples, with five cycles at 0.2 C, 1 C, 2 C, 5 C and 10 C rates and then back to 0.2 C. The discharge capacities at each rate are enhanced after co-doping, suggesting that the rate performance is improved after co-doping. The 10 C discharge capacities for LNMO, LNMO-Fe0.01, LNMO-FeP0.02, LNMO-FeP0.03, LNMO-FeP0.04 and LNMO-FeP0.05 are 111.7, 116.4, 125.2, 132.3, 134.6 and 122.8  $\text{mAh g}^{-1}$ . That is, LNMO-FeP0.04 displays the optimal rate capability among the co-doped samples. When  $x \leq 0.04$ , the gradually improved rate capability is mainly induced by the smaller primary particles, higher crystallinity, lower agglomeration and exposure of high-energy (110) and (311) crystal planes. The smaller primary particles may enlarge the electrode/electrolyte contact area and make the  $\text{Li}^+$  ions' diffusion path shorter. The increased exposure of high-energy (110) and (311) crystal planes is more conductive to  $\text{Li}^+$  ion diffusion [12]. The optimal rate capability of the LNMO-FeP0.04 sample is mainly attributed to the greater exposure of the (110) and (311) crystal planes. As  $x$  further increases to 0.05, the rate performance deteriorates adversely due to the lower  $\text{Mn}^{3+}$  content and the reduction or disappearance of the (311) and (110) crystal planes.

The cycling performance test was conducted on the un-doped and co-doped samples at 1 C and 25 °C, as shown in Figure 3c. The gradual decrease in discharge capacities with the cycle number is mainly ascribed to interfacial side reactions between the electrode and electrolyte and the accompanying continual growth of a CEI (Cathode–Electrolyte Interphase) layer on the electrode surface. The capacity retention rates are 76.7%, 80.9%, 85.9%, 88.8%, 83.1% and 78.6%, respectively, for LNMO, LNMO-Fe0.01, LNMO-FeP0.02, LNMO-FeP0.03, LNMO-FeP0.04 and LNMO-FeP0.05 after 200 cycles. It is evident that the cycling performance is obviously improved after  $\text{PO}_4^{3-}/\text{Fe}^{3+}$  co-doping. The LNMO-FeP0.03 sample exhibits the optimal cycling performance. When the co-doping amount  $x \leq 0.03$ , the cycling performance is gradually enhanced because of the reduced  $\text{Mn}^{3+}$  content and the decreased (111) crystal plane. A lower  $\text{Mn}^{3+}$  content may reduce the Jahn–Teller effect and  $\text{Mn}^{2+}$  dissolution during cycling [22]. In addition, the crystal planes contacting the electrolyte greatly affect the cycling capability of the LNMO material [28]. The (111) crystal plane has been reported to accelerate  $\text{Mn}^{2+}$  dissolution and demonstrate unstable interface behaviors at a high voltage, thereby adversely affecting the cycling capability of the LNMO material [28,29]. Therefore, increased exposure of the (111) crystal plane is disadvantageous to the cycling performance of the LNMO material. On the other hand, stronger Fe-O and P-O bonds can make the crystal structure more stable and reduce lattice stress during cycling, which is also conductive to the cycling performance of the LNMO material. However, a further increase in the co-doping amount leads to a decline in the cycling capability of LNMO-FeP0.04 and LNMO-FeP0.05, probably because of the lattice distortion caused by excessive doping disrupting the crystal structure stability. Additionally, the increased agglomeration and decreased  $\text{Mn}^{3+}$  content are also detrimental to the cycling performance of the LNMO-FeP0.04 and LNMO-FeP0.05 samples.

Figure 4 shows the CV curves obtained at different scan rates. Due to the limitations of  $\text{Li}^+$  diffusion dynamics, the oxidation/reduction peaks of all electrodes shift towards higher and lower potentials, respectively, as the scan rate increases. As shown in the insets of Figure 4a–f, the peak current ( $i_p$ ) of the oxidation/reduction peaks exhibits a linear

relation with the square root of the scan rate ( $v^{1/2}$ ). The Li<sup>+</sup> diffusion coefficient ( $D_{\text{Li}}$ ) for each redox peak can be obtained based on the Randles–Sevcik equation [30]:

$$i_p = (2.69 \times 10^5) n^{3/2} A D_{\text{Li}}^{1/2} v^{1/2} C_0 \quad (1)$$

where  $i_p$  is peak current (mA),  $n$  is 1,  $A$  is the electrode surface area (~1.13 cm<sup>2</sup>),  $v$  is the voltage scan rate (mV s<sup>-1</sup>), and  $C_0$  is the initial Li<sup>+</sup> ion concentration in the cathode (mol cm<sup>-3</sup>), which can be calculated according to the equation  $C_0 = 8/(N_A \cdot V)$ , where  $N_A$  is  $6.02 \times 10^{23}$ , and  $V$  is the refined lattice volume from the XRD pattern. The average Li<sup>+</sup> diffusion coefficient ( $D_a$ ) was obtained by averaging the four  $D_{\text{Li}}$  values, as shown in Table 2. The  $D_a$  values are  $1.084 \times 10^{-10}$ ,  $2.251 \times 10^{-10}$ ,  $3.609 \times 10^{-10}$ ,  $4.011 \times 10^{-10}$ ,  $4.582 \times 10^{-10}$  and  $2.594 \times 10^{-10}$  cm<sup>2</sup> s<sup>-1</sup>, respectively, for LNMO, LNMO-Fe0.01, LNMO-Fe0.02, LNMO-Fe0.03, LNMO-Fe0.04 and LNMO-Fe0.05. Evidently, all the co-doped samples exhibit higher Li<sup>+</sup> diffusion coefficients than the un-doped ones, which is attributable to improved crystallinity, reduced agglomeration, smaller primary particle size and a higher proportion of exposed (110) and (311) crystal planes. Compared to the (111) and (110) planes, the (110) and (311) planes expedite Li<sup>+</sup> ion diffusion during the cycling process [28], leading to a better rate capability of LNMO materials with more (110) and (311) planes, which accounts for the largest Li<sup>+</sup> ion diffusion coefficient of LNMO-Fe0.04. However, when  $x = 0.05$ , the Li<sup>+</sup> diffusion coefficient decreases significantly, possibly due to the disappearance of the (110) and (311) planes and increased agglomeration.

**Table 2.** Li<sup>+</sup> ions diffusion coefficients ( $D_{\text{Li}}$ ) for un-doped and co-doped samples.

Sample	$D_{\text{Li}} (\times 10^{-10} \text{ cm}^2 \text{ s}^{-1})$				$D_a (\times 10^{-10} \text{ cm}^2 \text{ s}^{-1})$
	O <sub>1</sub>	R <sub>1</sub>	O <sub>2</sub>	R <sub>2</sub>	
LNMO	0.497	1.694	1.327	0.817	1.084
LNMO-FeP0.01	1.947	3.933	2.027	1.098	2.251
LNMO-FeP0.02	2.039	2.959	6.136	3.302	3.609
LNMO-FeP0.03	3.665	6.502	2.606	3.269	4.011
LNMO-FeP0.04	1.694	6.058	6.850	3.725	4.582
LNMO-FeP0.05	1.565	4.745	1.410	2.657	2.594

To further determine the improved cycling capability of the co-doped samples, the EIS was tested to observe the impedance change after 50, 100, 150 and 200 cycles. Figure 5 shows the obtained Nyquist plots and fitting curves. All plots comprise two semicircles and a sloping line, representing the resistance of Li<sup>+</sup> ions passing through the electrode surface film ( $R_{\text{sf}}$ ), charge transfer resistance ( $R_{\text{ct}}$ ) and Warburg resistance associated with Li<sup>+</sup> ion diffusion in the electrode bulk ( $Z_w$ ). Manthiram et al. [31] pointed out that  $R_{\text{sf}}$  and  $R_{\text{ct}}$  include surface film and charge transfer resistances from the cathode and Li anode. Because the Li anode goes through the same electrochemical process before the EIS test, the obtained  $R_{\text{sf}}$  and  $R_{\text{ct}}$  values can roughly represent the resistances from the cathode. Table 3 lists the fitted  $R_{\text{sf}}$  and  $R_{\text{ct}}$  values, obtained using ZView2 software, according to the equivalent circuit in the inset of Figure 5. For all electrodes, the gradual increase in  $R_{\text{sf}}$  with the cycle number may be caused by the continual side reactions and CEI growth. However, after different cycle numbers, the  $R_{\text{sf}}$  of co-doped samples is decreased compared to the un-doped sample, implying the effectively inhibited side reactions and CEI growth after co-doping. On one hand, stronger Fe-O and P-O bonds have a strong inhibitory effect on lattice distortion during cycling. On the other hand, the exposed crystal planes also affect interfacial side reactions. The exposure of more (110) and (311) crystal planes could reduce interfacial side reactions, thereby decreasing interfacial impedance. Additionally, when the co-doping amount  $x = 0.03$ , the LNMO-FeP0.03 sample exhibits the lowest  $R_{\text{sf}}$  values due to its higher proportion of exposed (110) and (311) planes and moderate agglomeration. However, when  $x \geq 0.04$ , the particle agglomeration rates of the samples increase, and the (110) and (311) crystal planes gradually decrease until their disappearance at  $x = 0.05$ , thus

leading to increased side reactions. Consequently, LNMO-FeP0.04 and LNMO-FeP0.05 exhibit higher  $R_{sf}$  values than LNMO-FeP0.03.

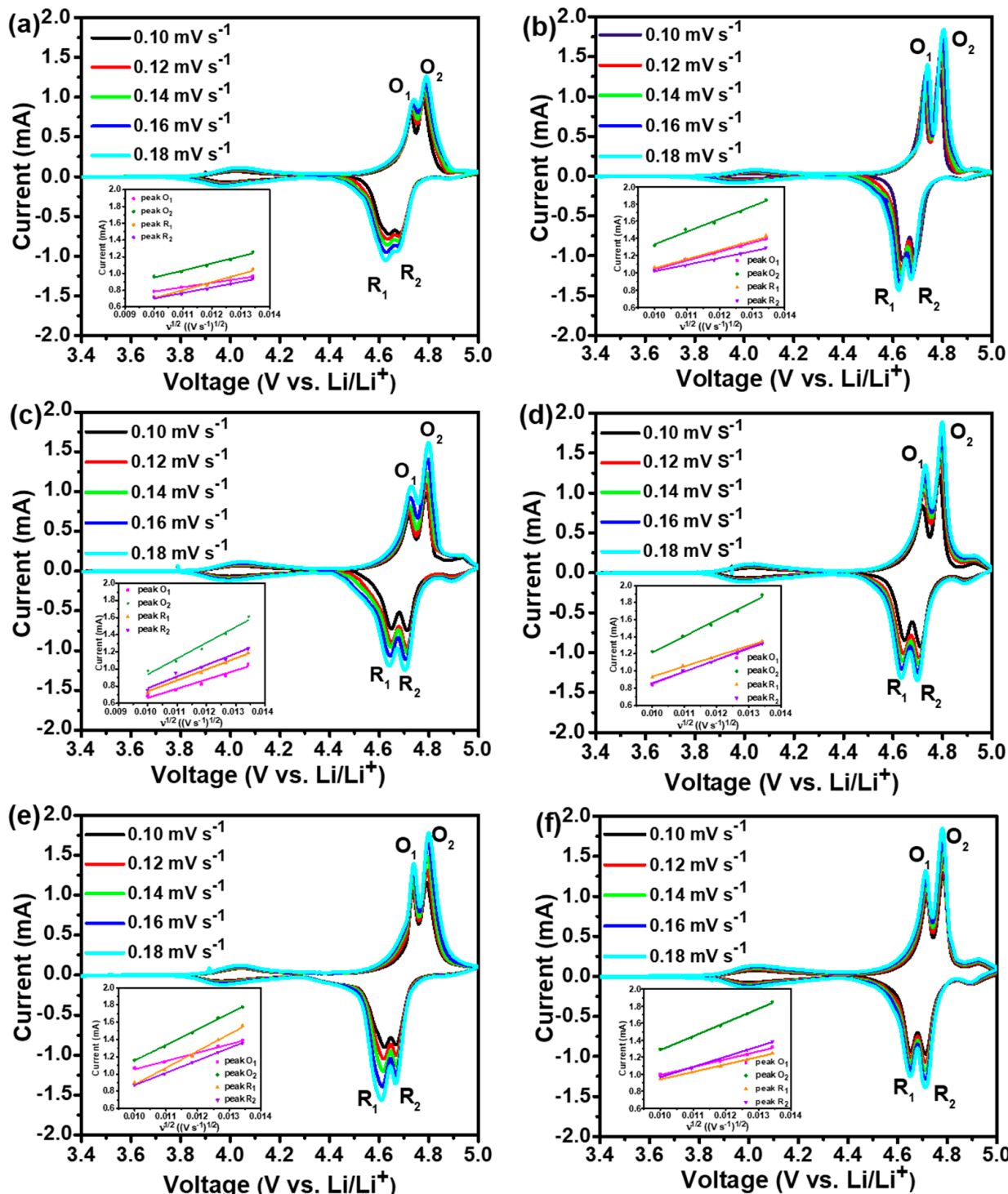


**Figure 4.** CV curves obtained at different scan rates and linear relationship between peak current and square root of scan rates for un-doped and co-doped samples: (a) LNMO, (b) LNMO-FeP0.01, (c) LNMO-FeP0.02, (d) LNMO-FeP0.03, (e) LNMO-FeP0.04, (f) LNMO-FeP0.05.

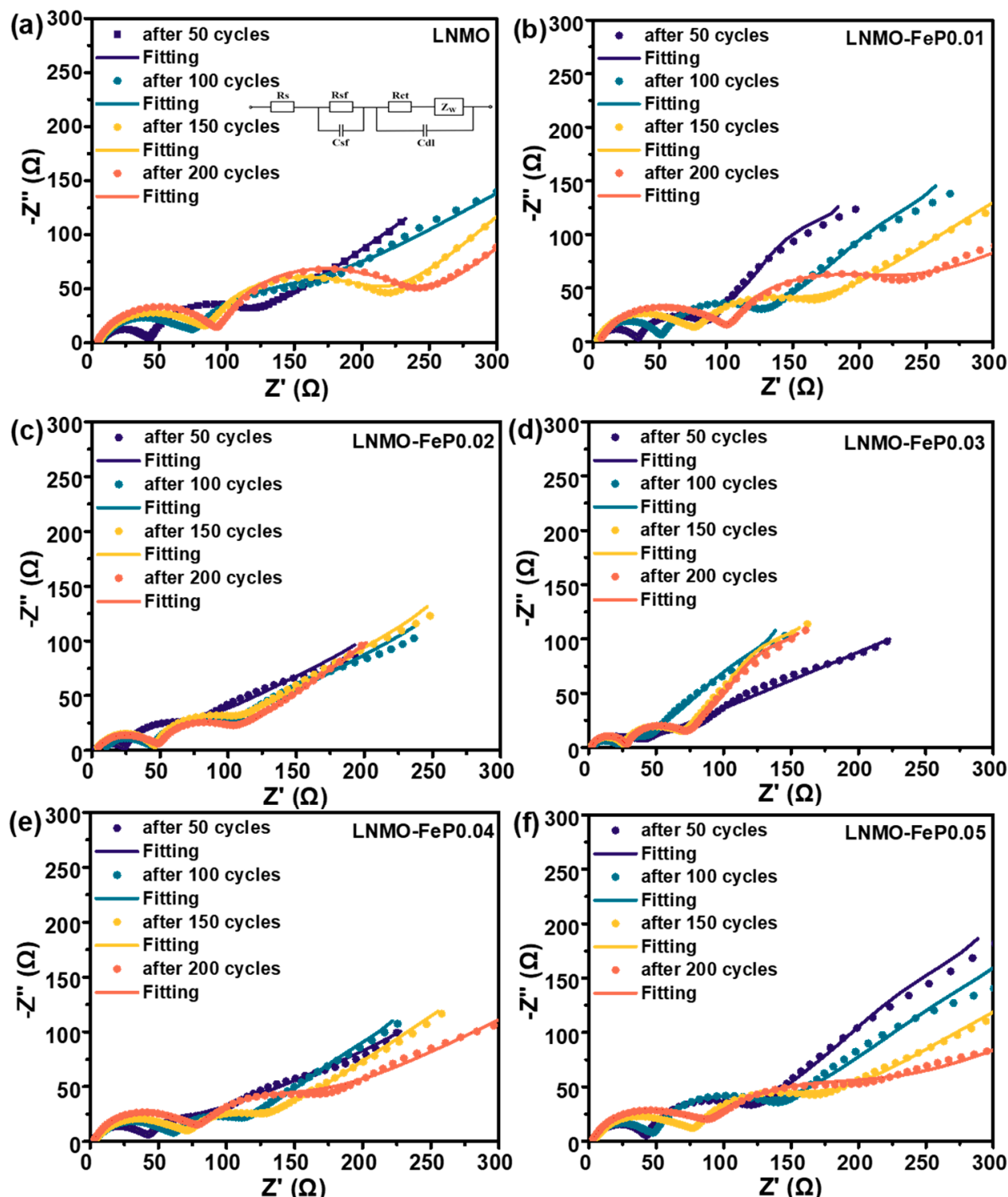


**Figure 5.** Nyquist plots and fitting lines after different cycle numbers for un-doped and co-doped samples: (a) LNMO, (b) LNMO-FeP0.01, (c) LNMO-FeP0.02, (d) LNMO-FeP0.03, (e) LNMO-FeP0.04, (f) LNMO-FeP0.05.

In addition, the  $R_{ct}$  values after 50, 100, 150 and 200 cycles are also compared in Table 3, showing a gradually increasing trend with cycling. Among them, the LNMO-FeP0.03 electrode displays smaller  $R_{ct}$  values during the whole cycle process, suggesting its faster electrochemical kinetics, maybe due to the fewer interfacial side reactions.

**Table 3.** Fitted  $R_{sf}$  and  $R_{ct}$  values according to Figure 5a–f.

Sample	Resistance ( $\Omega$ )	After 50 Cycles	After 100 Cycles	After 150 Cycles	After 200 Cycles
LNMO	$R_{sf}$	38.56	68.16	79.70	91.11
	$R_{ct}$	65.22	72.16	123.70	136.20
LNMO-FeP0.01	$R_{sf}$	30.60	49.26	72.25	97.14
	$R_{ct}$	49.37	68.34	78.01	92.70
LNMO-FeP0.02	$R_{sf}$	21.75	36.36	44.34	46.70
	$R_{ct}$	34.54	36.04	43.86	48.64
LNMO-FeP0.03	$R_{sf}$	12.48	18.84	24.09	25.71
	$R_{ct}$	15.60	24.38	41.57	43.21
LNMO-FeP0.04	$R_{sf}$	38.74	57.52	66.39	74.19
	$R_{ct}$	26.65	45.79	52.78	65.52
LNMO-FeP0.05	$R_{sf}$	39.10	44.73	72.28	78.66
	$R_{ct}$	70.32	77.62	84.31	114.50

#### 4. Conclusions

$\text{LiNi}_{0.5}\text{Mn}_{1.5}\text{O}_4$  materials with different  $\text{PO}_4^{3-}/\text{Fe}^{3+}$  co-doping amounts have been synthesized using a combined coprecipitation–hydrothermal method along with high-temperature calcination. The results reveal that the Ni/Mn disordering degree and  $\text{Mn}^{3+}$  content gradually decrease with the co-doping amounts. SEM observations show that the particle morphology of the samples is influenced significantly by the co-doping amounts. The aggregation degree first decreases and then increases with the co-doping amounts. Additionally, when the co-doping amount  $x \leq 0.04$ , high-energy (110) and (311) crystal planes gradually increase with increasing co-doping amounts. However, when the co-doping amount increases to  $x = 0.05$ , the (311) and (110) crystal planes gradually decrease or even disappear. Electrochemical tests demonstrate that the  $\text{LiNi}_{0.5}\text{Mn}_{1.45}\text{Fe}_{0.03}\text{P}_{0.02}\text{O}_4$  sample ( $x = 0.03$ ) exhibits the best cycling stability, and the  $\text{LiNi}_{0.5}\text{Mn}_{1.4333}\text{Fe}_{0.04}\text{P}_{0.0267}\text{O}_4$  ( $x = 0.04$ ) sample exhibits the optimal rate performance. This co-doping strategy can also be adopted to other cathode materials to achieve an intriguing electrochemical performance.

**Author Contributions:** Y.W. and S.F. contributed equally to this work. Conceptualization, methodology and software, S.F.; formal analysis, Y.W.; data curation, X.D.; resources, D.W.; writing—review and editing, J.Z. and L.W.; funding acquisition, L.W.; supervision, G.L. All authors have read and agreed to the published version of the manuscript.

**Funding:** This research was funded by the National Natural Science Foundation of China, grant number [No. 51802074].

**Data Availability Statement:** The raw data supporting the conclusions of this article will be made available by the authors on request.

**Conflicts of Interest:** Authors Yong Wang, Xianzhen Du, Dong Wei, Jingpeng Zhang and Guangchuan Liang were employed by the company Shandong Goldencell Electronics Technology Co., Ltd. The remaining authors declare that the research was conducted in the absence of any commercial or financial relationships that could be construed as a potential conflict of interest.

#### References

- Qian, H.; Ren, H.; Zhang, Y.; He, X.; Li, W.; Wang, J.; Hu, J.; Yang, H.; Sari, H.M.K.; Chen, Y.; et al. Surface doping vs. bulk doping of cathode materials for lithium-ion batteries: A review. *Electrochem. Energy Rev.* **2022**, *5*, 2. [[CrossRef](#)]
- Yi, H.; Liang, Y.; Qian, Y.; Feng, Y.; Li, Z.; Zhang, X. Low-cost Mn-based cathode materials for lithium-ion batteries. *Batteries* **2023**, *9*, 246. [[CrossRef](#)]
- Wu, W.; Zuo, S.; Zhang, X.; Feng, X. Two-step solid state synthesis of medium entropy  $\text{LiNi}_{0.5}\text{Mn}_{1.5}\text{O}_4$  cathode with enhanced electrochemical performance. *Batteries* **2023**, *9*, 91. [[CrossRef](#)]

4. Wang, B.; Son, S.-B.; Badami, P.; Trask, S.E.; Abraham, D.; Qin, Y.; Yang, Z.; Wu, X.; Jansen, A.; Liao, C. Understanding and mitigating the dissolution and delamination issues encountered with high-voltage  $\text{LiNi}_{0.5}\text{Mn}_{1.5}\text{O}_4$ . *Batteries* **2023**, *9*, 435. [[CrossRef](#)]
5. Ma, C.; Wen, Y.; Qiao, Q.; He, P.; Ren, S.; Li, M.; Zhao, P.; Qiu, J.; Tang, G. Improving electrochemical performance of high-voltage spinel  $\text{LiNi}_{0.5}\text{Mn}_{1.5}\text{O}_4$  cathodes by silicon oxide surface modification. *ACS Appl. Energy Mater.* **2021**, *4*, 12201–12210. [[CrossRef](#)]
6. Yu, C.; Dong, L.; Zhang, Y.; Du, K.; Gao, M.; Zhao, H.; Bai, Y. Promoting electrochemical performances of  $\text{LiNi}_{0.5}\text{Mn}_{1.5}\text{O}_4$  cathodes via  $\text{YF}_3$  surface coating. *Solid State Ion.* **2020**, *357*, 115464. [[CrossRef](#)]
7. Wu, Y.; Ben, L.; Zhan, Y.; Yu, H.; Qi, W.; Zhao, W.; Huang, X. Binding  $\text{Li}_3\text{PO}_4$  to spinel  $\text{LiNi}_{0.5}\text{Mn}_{1.5}\text{O}_4$  via a surface Co-containing bridging layer to improve the electrochemical performance. *Energy Technol.* **2021**, *9*, 2100147. [[CrossRef](#)]
8. Mou, J.R.; Deng, Y.L.; He, L.H.; Zheng, Q.J.; Jiang, N.; Lin, D.M. Critical roles of semi-conductive  $\text{LaFeO}_3$  coating in enhancing cycling stability and rate capability of 5 V  $\text{LiNi}_{0.5}\text{Mn}_{1.5}\text{O}_4$  cathode materials. *Electrochim. Acta* **2018**, *260*, 101–111. [[CrossRef](#)]
9. Mereacre, V.; Stüble, P.; Trouillet, V.; Ahmed, S.; Volz, K.; Binder, J.R. Coating versus doping: Understanding the enhanced performance of high-voltage batteries by the coating of spinel  $\text{LiNi}_{0.5}\text{Mn}_{1.5}\text{O}_4$  with  $\text{Li}_{0.35}\text{La}_{0.55}\text{TiO}_3$ . *Adv. Mater. Interfaces* **2023**, *10*, 2201324. [[CrossRef](#)]
10. Wang, J.; Chen, D.; Wu, W.; Wang, L.; Liang, G. Effects of  $\text{Na}^+$  doping on crystalline structure and electrochemical performances of  $\text{LiNi}_{0.5}\text{Mn}_{1.5}\text{O}_4$  cathode material. *Trans. Nonferrous Met. Soc. China* **2017**, *27*, 2239–2248. [[CrossRef](#)]
11. Liang, G.; Wu, Z.; Didier, C.; Zhang, W.; Cuan, J.; Li, B.; Ko, K.-Y.; Hung, P.-Y.; Lu, C.-Z.; Chen, Y.; et al. A long cycle-life high-voltage spinel lithium-ion battery electrode achieved by site-selective doping. *Angew. Chem. Int. Ed.* **2020**, *59*, 10594–10602. [[CrossRef](#)] [[PubMed](#)]
12. Hsiao, Y.-S.; Huang, J.-H.; Cheng, T.-H.; Hu, C.-W.; Wu, N.-J.; Yen, C.-Y.; Hsu, S.-C.; Weng, H.C.; Chen, C.-P. Cr-doped  $\text{LiNi}_{0.5}\text{Mn}_{1.5}\text{O}_4$  derived from bimetallic Ni/Mn metal-organic framework as high-performance cathode for lithium-ion batteries. *J. Energy Storage* **2023**, *68*, 107686. [[CrossRef](#)]
13. Zhou, D.; Li, J.; Chen, C.; Lin, F.; Wu, H.; Guo, J. A hydrothermal synthesis of Ru-doped  $\text{LiMn}_{1.5}\text{Ni}_{0.5}\text{O}_4$  cathode materials for enhanced electrochemical performance. *RSC Adv.* **2021**, *11*, 12549. [[CrossRef](#)]
14. Luo, Y.; Li, H.; Lu, T.; Zhang, Y.; Mao, S.S.; Liu, Z.; Wen, W.; Xie, J.; Yan, L. Fluorine gradient-doped  $\text{LiNi}_{0.5}\text{Mn}_{1.5}\text{O}_4$  spinel with improved high voltage stability for Li-ion batteries. *Electrochim. Acta* **2017**, *238*, 237–245. [[CrossRef](#)]
15. Kim, D.-W.; Zettsu, N.; Shiiba, H.; Sánchez-Santolino, G.; Ishikawa, R.; Ikuhara, Y.; Teshima, K. Metastable oxysulfide surface formation on  $\text{LiNi}_{0.5}\text{Mn}_{1.5}\text{O}_4$  single crystal particles by carbothermal reaction with sulfur-doped heterocarbon nanoparticles: New insight into their structural and electrochemical characteristics, and their potential applications. *J. Mater. Chem. A* **2020**, *8*, 22302–22314.
16. Kim, W.-K.; Han, D.-W.; Ryu, W.-H.; Lim, S.-J.; Eom, J.-Y.; Kwon, H.-S. Effects of Cl doping on the structural and electrochemical properties of high voltage  $\text{LiMn}_{1.5}\text{Ni}_{0.5}\text{O}_4$  cathode materials for Li-ion batteries. *J. Alloys Compd.* **2014**, *592*, 48–52. [[CrossRef](#)]
17. Chen, T.; Li, X.; Wang, H.; Yan, X.; Wang, L.; Deng, B.; Ge, W.; Qu, M. The effect of gradient boracic polyanion-doping on structure, morphology, and cycling performance of Ni-rich  $\text{LiNi}_{0.8}\text{Co}_{0.15}\text{Al}_{0.05}\text{O}_2$  cathode material. *J. Power Sources* **2018**, *374*, 1–11. [[CrossRef](#)]
18. Yang, G.; Pan, K.; Lai, F.; Wang, Z.; Chu, Y.; Yang, S.; Han, J.; Wang, H.; Zhang, X.; Li, Q. Integrated co-modification of  $\text{PO}_4^{3-}$  polyanion doping and  $\text{Li}_2\text{TiO}_3$  coating for Ni-rich layered  $\text{LiNi}_{0.6}\text{Co}_{0.2}\text{Mn}_{0.2}\text{O}_2$  cathode material of lithium-ion batteries. *Chem. Eng. J.* **2021**, *421*, 129964. [[CrossRef](#)]
19. Zhang, H.-Z.; Li, F.; Pan, G.-L.; Li, G.-R.; Gao, X.-P. The effect of polyanion-doping on the structure and electrochemical performance of Li-rich layered oxides as cathode for lithium-ion batteries. *J. Electrochem. Soc.* **2015**, *162*, A1899–A1904. [[CrossRef](#)]
20. Fu, S.; Zhang, Y.; Bian, Y.; Xu, J.; Wang, L.; Liang, G. Effect of  $\text{Fe}^{3+}$  and/or  $\text{PO}_4^{3-}$  doping on the electrochemical performance of  $\text{LiNi}_{0.5}\text{Mn}_{1.5}\text{O}_4$  cathode material for Li-ion batteries. *Ind. Eng. Chem. Res.* **2023**, *62*, 1016–1028. [[CrossRef](#)]
21. Lan, L.; Li, S.; Li, J.; Lu, L.; Lu, Y.; Huang, S.; Xu, S.; Pan, C.; Zhao, F. Enhancement of the electrochemical performance of the spinel structure  $\text{LiNi}_{0.5-x}\text{Ga}_x\text{Mn}_{1.5}\text{O}_4$  cathode material by Ga doping. *Nanoscale Res. Lett.* **2018**, *13*, 251. [[CrossRef](#)] [[PubMed](#)]
22. Gong, J.; Fu, S.; Zhang, Y.; Yan, S.; Lang, Y.; Guo, J.; Wang, L.; Liang, G. Enhanced electrochemical performance of 5V  $\text{LiNi}_{0.5}\text{Mn}_{1.5-x}\text{Zr}_x\text{O}_4$  cathode material for lithium-ion batteries. *ChemistrySelect* **2021**, *6*, 7202–7212. [[CrossRef](#)]
23. Liu, D.; Hamel-Paquet, J.; Trottier, J.; Baray, F.; Gariépy, V.; Hovington, P.; Guerfi, A.; Mauger, A.; Julien, C.M.; Goodenough, J.B.; et al. Synthesis of pure phase disordered  $\text{LiMn}_{1.45}\text{Cr}_{0.1}\text{Ni}_{0.45}\text{O}_4$  by a post-annealing method. *J. Power Sources* **2012**, *217*, 400–406. [[CrossRef](#)]
24. Kunduraci, M.; Amatucci, G.G. Synthesis and characterization of nanostructured 4.7 V  $\text{Li}_x\text{Mn}_{1.5}\text{Ni}_{0.5}\text{O}_4$  spinels for high-power lithium-ion batteries. *J. Electrochem. Soc.* **2006**, *153*, A1345–A1352. [[CrossRef](#)]
25. Kim, J.-H.; Myung, S.-T.; Yoon, C.S.; Kang, S.G.; Sun, Y.-K. Comparative study of  $\text{LiNi}_{0.5}\text{Mn}_{1.5}\text{O}_{4-\delta}$  and  $\text{LiNi}_{0.5}\text{Mn}_{1.5}\text{O}_4$  cathodes having two crystallographic structures:  $Fd\bar{3}m$  and  $P4_332$ . *Chem. Mater.* **2004**, *16*, 906–914. [[CrossRef](#)]
26. Zheng, X.; Liu, W.; Qu, Q.; Zheng, H.; Huang, Y. Bi-functions of titanium and lanthanum co-doping to enhance the electrochemical performance of spinel  $\text{LiNi}_{0.5}\text{Mn}_{1.5}\text{O}_4$  cathode. *J. Mater.* **2019**, *5*, 156–163. [[CrossRef](#)]
27. Zeng, Y.-P.; Wu, X.-I.; Mei, P.; Cong, L.-N.; Yao, C.; Wang, R.-S.; Xie, H.-M.; Sun, L.-Q. Effect of cationic and anionic substitutions on the electrochemical properties of  $\text{LiNi}_{0.5}\text{Mn}_{1.5}\text{O}_4$  spinel cathode materials. *Electrochim. Acta* **2014**, *138*, 493–500. [[CrossRef](#)]

28. Liu, H.; Wang, J.; Zhang, X.; Zhou, D.; Qi, X.; Qiu, B.; Fang, J.; Kloepsch, R.; Schumacher, G.; Liu, Z.; et al. Morphological evolution of high-voltage spinel  $\text{LiNi}_{0.5}\text{Mn}_{1.5}\text{O}_4$  cathode materials for lithium-ion batteries: The critical effects of surface orientations and particle size. *ACS Appl. Mater. Interfaces* **2016**, *8*, 4661–4675. [[CrossRef](#)]
29. Chen, Z.; Zhao, R.; Du, P.; Hu, H.; Wang, T.; Zhu, L.; Chen, H. Polyhedral  $\text{LiNi}_{0.5}\text{Mn}_{1.5}\text{O}_4$  with excellent electrochemical properties for lithium-ion batteries. *J. Mater. Chem. A* **2014**, *2*, 12835–12848. [[CrossRef](#)]
30. Liu, W.; Li, X.; Xiong, D.; Hao, Y.; Li, J.; Kou, H.; Yan, B.; Li, D.; Lu, S.; Koo, A.; et al. Significantly improving cycling performance of cathodes in lithium ion batteries: The effect of  $\text{Al}_2\text{O}_3$  and  $\text{LiAlO}_2$  coatings on  $\text{LiNi}_{0.6}\text{Co}_{0.2}\text{Mn}_{0.2}\text{O}_2$ . *Nano Energy* **2018**, *44*, 111–120. [[CrossRef](#)]
31. Liu, J.; Manthiram, A. Understanding the improved electrochemical performances of Fe-substituted 5 V spinel cathode  $\text{LiMn}_{1.5}\text{Ni}_{0.5}\text{O}_4$ . *J. Phys. Chem. C* **2009**, *113*, 15073–15079. [[CrossRef](#)]

**Disclaimer/Publisher’s Note:** The statements, opinions and data contained in all publications are solely those of the individual author(s) and contributor(s) and not of MDPI and/or the editor(s). MDPI and/or the editor(s) disclaim responsibility for any injury to people or property resulting from any ideas, methods, instructions or products referred to in the content.